IEEE Access
Multidisciplinary | Rapid Review | Open Access Journal

Received September 27, 2020, accepted October 14, 2020, date of publication October 27, 2020, date of current version November 4, 2020.

Digital Object Identifier 10.1109/ACCESS.2020.3033409

Comparing Combinations of Linear and Nonlinear Feedback Terms for Ship Motion Control

MIKKEL ESKE NØRGAARD SØRENSEN[1,2], MORTEN BREIVIK[1,2], (Member, IEEE), AND ROGER SKJETNE[1,3], (Member, IEEE)

[1]Centre for Autonomous Marine Operations and Systems, Norwegian University of Science and Technology (NTNU), 7491 Trondheim, Norway
[2]Department of Engineering Cybernetics, Norwegian University of Science and Technology (NTNU), 7491 Trondheim, Norway
[3]Department of Marine Technology, Norwegian University of Science and Technology (NTNU), 7491 Trondheim, Norway

Corresponding author: Mikkel Eske Nørgaard Sørensen (mikkel.e.n.sorensen@ieee.org)

This work was supported by the Research Council of Norway through the Centres of Excellence Funding Scheme under Project 223254.

ABSTRACT In this article, combinations of linear and nonlinear feedback terms are investigated for 3 degrees-of-freedom pose and velocity control of ships. Nonlinear control algorithms that are found in the literature often have linear feedback terms, which result in nice globally exponential stability properties when assuming no actuator constraints. However, considering that all actuators have saturation constraints, such stability properties are not feasible in practice. Applying nonlinear feedback terms can be a step to handle such constraints. As a result, this article explores nonlinear feedback terms for both the kinematic and kinetic control loops. Specifically, three controllers based on a cascaded backstepping control design are implemented and compared through simulations and model-scale experiments in an ocean basin. Stability properties and tuning rules for all the controllers are also provided. Interestingly, the use of nonlinear feedback terms gives the ability to constrain the feedback control inputs globally while simultaneously being able to change the convergence rates locally. The price to be paid is the introduction of additional tuning parameters. The three controller types are compared using performance metrics which consider both control accuracy and energy use.

INDEX TERMS Ship motion control, dynamic positioning, cascaded backstepping control design, nonlinear feedback terms, tuning rules, performance metrics, experimental results.

I. INTRODUCTION

Automatic motion control of ships has been an active research topic since the early 20th century [1]. In recent years, the research has expanded from control of manned ships to also include unmanned ships. In this regard, many ship motion control algorithms found in the literature do not take into account saturation constraints for the actuators. For example, the nonlinear control algorithms in [2]–[5] and [6] are all designed with linear feedback terms.

This article therefore investigates the use of nonlinear feedback terms, and in particular the use of combinations of linear and nonlinear feedback terms for 3 degrees-of-freedom (DOFs) pose and velocity control of ships. These feedback terms are developed based on constant bearing (CB) guidance principles, inspired by the guided dynamic positioning approach originally suggested in [7], and further developments on the concept of guided motion control as explored in [8] and [9].

Specifically, this article is a further development of the work in [10], concerning the development of three 3-DOFs motion controllers based on a cascaded backstepping control design, where the feedback connection between pose and velocity, traditionally found in backstepping designs as in [2] and [5], has been removed. The considered controllers respectively employ linear feedback for both the pose and velocity control errors (LP-LV), nonlinear feedback for the pose control error and linear feedback for the velocity control error (NP-LV), as well as nonlinear feedback for both the pose and velocity control errors (NP-NV). Compared to [10], this article presents stability properties associated with all the controllers, suggests suitable tuning rules, and evaluates the controller performance through new simulations and model-scale experiments using a so-called 4-corner test. For this, the LP-LV controller is used as a baseline controller. Specifically, the controllers are compared using performance

The associate editor coordinating the review of this manuscript and approving it for publication was Chao-Yang Chen.

metrics which consider both control accuracy and energy use. Additional work considering the nonlinear feedback controllers from [10] is presented in [11], where a magnitude-rate saturation (MRS) model is added to the system and the effects are explored through model-scale experiments. Other recent work which consider the use of nonlinear feedback terms include [12] and [11], where sine and arctan functions, respectively, are employed for the purpose of 1-DOF ship heading control. In [14], an adaptive fuzzy tracking algorithm was proposed for vessel motion control to handle external disturbances. However, such adaptive mechanisms make it difficult to trace the resulting vessel performance back to the detailed behavior of the feedbacks and is therefore not directly comparable to the studied feedbacks of this article.

The structure of the rest of the paper is as follows: A mathematical ship model and relevant assumptions are presented in Section II; Section III presents the design of three cascaded control laws based on backstepping and CB guidance; Section IV proposes a set of tuning rules; Section V includes simulation results, experimental results and a performance comparison; while Section VI concludes the paper.

II. SHIP MODEL

The horizontal motion of a ship can be represented by the pose vector $\boldsymbol{\eta} = [x, y, \psi]^\top \in \mathbb{R}^2 \times \mathbb{S}$ and the velocity vector $\boldsymbol{\nu} = [u, v, r]^\top \in \mathbb{R}^3$, where $\mathbb{S} = [-\pi, \pi)$. Here, (x, y) represents the Cartesian position in the local earth-fixed reference frame, ψ is the yaw angle, (u, v) represents the body-fixed linear velocities, and r is the yaw rate. The 3 degrees-of-freedom (DOFs) dynamics of a ship is then stated as [5]:

$$\dot{\boldsymbol{\eta}} = \mathbf{R}(\psi)\boldsymbol{\nu} \tag{1}$$

$$\mathbf{M}\dot{\boldsymbol{\nu}} + \mathbf{C}(\boldsymbol{\nu})\boldsymbol{\nu} + \mathbf{D}(\boldsymbol{\nu})\boldsymbol{\nu} = \boldsymbol{\tau}, \tag{2}$$

where

$$\mathbf{R}(\psi) = \begin{bmatrix} \cos(\psi) & -\sin(\psi) & 0 \\ \sin(\psi) & \cos(\psi) & 0 \\ 0 & 0 & 1 \end{bmatrix} \tag{3}$$

is a rotation matrix $\mathbf{R} \in SO(3)$, while $\mathbf{M}$, $\mathbf{C}(\boldsymbol{\nu})$, $\mathbf{D}(\boldsymbol{\nu})$, and $\boldsymbol{\tau}$ represent the inertia matrix, Coriolis and centripetal matrix, damping matrix, and control input vector, respectively. The system matrices are assumed to satisfy the properties $\mathbf{M} = \mathbf{M}^\top > 0$, $\mathbf{C}(\boldsymbol{\nu}) = -\mathbf{C}(\boldsymbol{\nu})^\top$, and $\mathbf{D}(\boldsymbol{\nu}) > 0$.

III. CONTROL DESIGN

The control objective is to make $\tilde{\boldsymbol{\eta}}(t) \triangleq \boldsymbol{\eta}(t) - \boldsymbol{\eta}_t(t) \to \mathbf{0}$ as $t \to \infty$, where $\boldsymbol{\eta}_t(t) = [x_t(t), y_t(t), \psi_t(t)]^\top \in \mathbb{R}^2 \times \mathbb{S}$ is $\mathcal{C}^2$ and bounded, representing the pose associated with a target point that is to be reached. The motion of the target is typically defined by a human or generated by a guidance system.

The control design is divided into two stages, including definition of new state variables and deriving the control laws through control Lyapunov functions (CLFs). The design is similar to the backstepping method, which has been applied in e.g. [2], [6] and [15], but omits the coupling between the pose and velocity control loops, which results in a cascaded system. Hence, we call this approach for cascaded backstepping control design. Such a decoupling is similar to what is achieved by using an LgV backstepping design [16]. The resulting cascaded system corresponds to a classical inner-outer loop guidance and control structure, where the outer loop handles the kinematics and the inner loop handles the kinetics. The total system is then analysed by cascade theory [17]. In particular, it is of interest to investigate the effect of using nonlinear feedback terms in the control loops. Consequently, we investigate three combinations of linear and nonlinear feedback terms. Fig. 1 shows a block diagram of these combinations.

For notational simplicity, the time t is omitted in the rest of this section.

A. LINEAR POSE AND VELOCITY FEEDBACKS (LP-LV)

We start by defining the error variables $\mathbf{z}_1$ and $\mathbf{z}_2$:

$$\mathbf{z}_1 \triangleq \mathbf{R}^\top(\psi)(\boldsymbol{\eta} - \boldsymbol{\eta}_t) \tag{4}$$

$$\mathbf{z}_2 \triangleq \boldsymbol{\nu} - \boldsymbol{\alpha}, \tag{5}$$

where $\boldsymbol{\alpha} \in \mathbb{R}^3$ is a vector of stabilising functions, which can be interpreted as a desired velocity to be designed.

1) KINEMATIC CONTROL

Choosing the positive definite CLF

$$V_1 \triangleq \frac{1}{2}\mathbf{z}_1^\top \mathbf{z}_1, \tag{6}$$

the derivative of V_1 with respect to time along the $\mathbf{z}_1$-dynamics gives

$$\begin{aligned} \dot{V}_1 &= \mathbf{z}_1^\top \dot{\mathbf{z}}_1 \\ &= \mathbf{z}_1^\top (\mathbf{S}(r)^\top \mathbf{R}^\top(\psi)(\boldsymbol{\eta} - \boldsymbol{\eta}_t) + \mathbf{R}^\top(\psi)(\dot{\boldsymbol{\eta}} - \dot{\boldsymbol{\eta}}_t)) \\ &= \mathbf{z}_1^\top (\mathbf{S}(r)^\top \mathbf{z}_1 + \mathbf{R}^\top(\psi)(\dot{\boldsymbol{\eta}} - \dot{\boldsymbol{\eta}}_t)), \end{aligned} \tag{7}$$

where

$$\mathbf{S}(r) = \begin{bmatrix} 0 & -r & 0 \\ r & 0 & 0 \\ 0 & 0 & 0 \end{bmatrix} = -\mathbf{S}(r)^\top \tag{8}$$

is a skew-symmetric matrix satisfying $\mathbf{z}_1^\top \mathbf{S}(r)^\top \mathbf{z}_1 = 0$, $\forall \mathbf{z}_1$. This gives

$$\dot{V}_1 = \mathbf{z}_1^\top (\boldsymbol{\nu} - \mathbf{R}^\top(\psi)\dot{\boldsymbol{\eta}}_t). \tag{9}$$

Using (5), the CLF becomes

$$\begin{aligned} \dot{V}_1 &= \mathbf{z}_1^\top (\mathbf{z}_2 + \boldsymbol{\alpha} - \mathbf{R}^\top(\psi)\dot{\boldsymbol{\eta}}_t) \\ &= \mathbf{z}_1^\top \mathbf{z}_2 + \mathbf{z}_1^\top (\boldsymbol{\alpha} - \mathbf{R}^\top(\psi)\dot{\boldsymbol{\eta}}_t), \end{aligned} \tag{10}$$

where the stabilising function can be chosen as

$$\boldsymbol{\alpha} = \mathbf{R}^\top(\psi)\dot{\boldsymbol{\eta}}_t - \boldsymbol{\Gamma}_1 \mathbf{z}_1 \tag{11}$$

with $\boldsymbol{\Gamma}_1 = \boldsymbol{\Gamma}_1^\top > 0$, resulting in

$$\dot{V}_1 = -\mathbf{z}_1^\top \boldsymbol{\Gamma}_1 \mathbf{z}_1 + \mathbf{z}_1^\top \mathbf{z}_2. \tag{12}$$

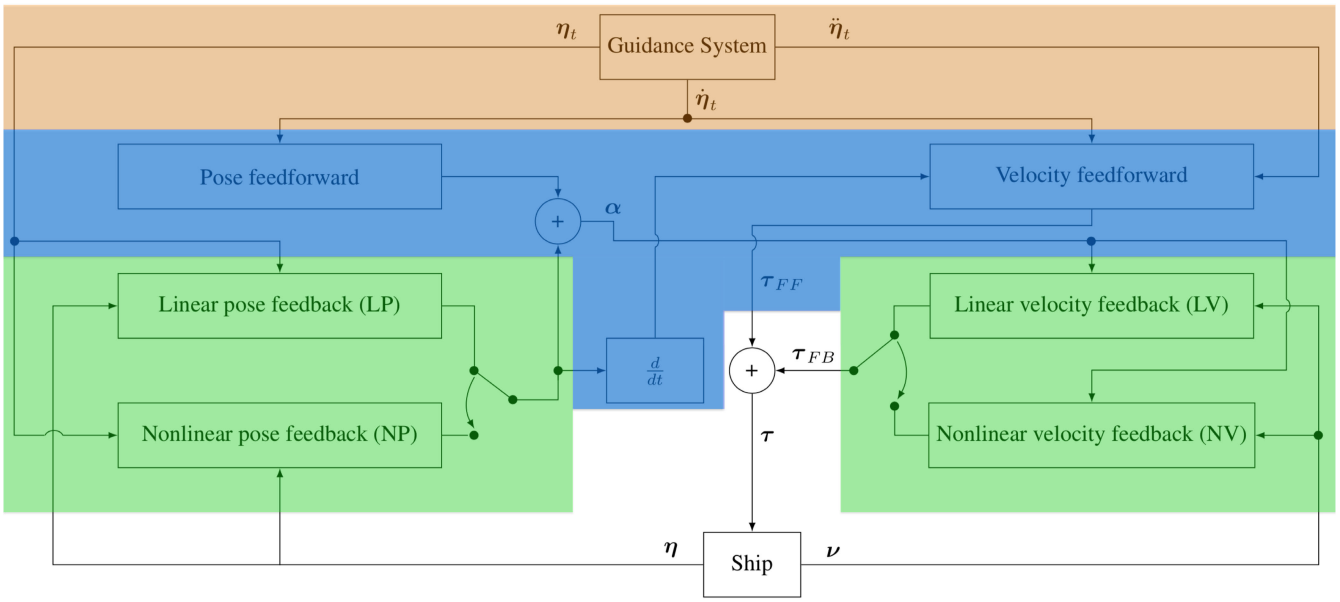

FIGURE 1. The possible combinations of the feedforward and feedback control loops considered in this article.

It can be concluded that the origin of $\mathbf{z}_1$ is uniformly globally exponentially stable (UGES) for $\mathbf{z}_2 = \mathbf{0}$. Consequently, it can be concluded by Lemma 4.6 in [18] that the subsystem

$$\dot{\mathbf{z}}_1 = \mathbf{S}(r)^\top \mathbf{z}_1 - \mathbf{\Gamma}_1 \mathbf{z}_1 + \mathbf{z}_2 \tag{13}$$

is input-to-state stable (ISS). Note that (12) shows that $\mathbf{S}(r)$ in (13) does not affect the ISS property.

2) KINETIC CONTROL

The $\mathbf{z}_2$-dynamics can be written as

$$\begin{aligned} \mathbf{M}\dot{\mathbf{z}}_2 &= \mathbf{M}(\dot{\boldsymbol{\nu}} - \dot{\boldsymbol{\alpha}}) \\ &= \boldsymbol{\tau} - \mathbf{C}(\boldsymbol{\nu})\boldsymbol{\nu} - \mathbf{D}(\boldsymbol{\nu})\boldsymbol{\nu} - \mathbf{M}\dot{\boldsymbol{\alpha}}, \end{aligned} \tag{14}$$

where the time derivative of (11) becomes

$$\dot{\boldsymbol{\alpha}} = \mathbf{R}^\top(\psi)\ddot{\boldsymbol{\eta}}_t + \mathbf{S}(r)^\top \mathbf{R}^\top(\psi)\dot{\boldsymbol{\eta}}_t - \mathbf{\Gamma}_1 \dot{\mathbf{z}}_1 \tag{15}$$

where $\boldsymbol{\eta}_t$ is the pose of the target point and $\dot{\mathbf{z}}_1$ is given by (13). The CLF for $\mathbf{z}_2$ is defined as

$$V_2 \triangleq \frac{1}{2}\mathbf{z}_2^\top \mathbf{M}\mathbf{z}_2. \tag{16}$$

Simplifying $\mathbf{C}(\boldsymbol{\nu}) = \mathbf{C}$, $\mathbf{D}(\boldsymbol{\nu}) = \mathbf{D}$, $\mathbf{R}(\psi) = \mathbf{R}$ and $\mathbf{S}(r) = \mathbf{S}$ for notational brevity, the derivative of (16) becomes

$$\begin{aligned} \dot{V}_2 &= \mathbf{z}_2^\top \mathbf{M}\dot{\mathbf{z}}_2 \\ &= \mathbf{z}_2^\top(\boldsymbol{\tau} - \mathbf{C}\boldsymbol{\nu} - \mathbf{D}\boldsymbol{\nu} - \mathbf{M}\dot{\boldsymbol{\alpha}}). \end{aligned} \tag{17}$$

The control input can now be chosen as

$$\begin{aligned} \boldsymbol{\tau} &= \boldsymbol{\tau}_{FF} + \boldsymbol{\tau}_{FB} && (18) \\ &= \mathbf{M}\dot{\boldsymbol{\alpha}} + \mathbf{C}\boldsymbol{\nu} + \mathbf{D}\boldsymbol{\nu} - \mathbf{\Gamma}_2\mathbf{z}_2, && (19) \end{aligned}$$

where $\boldsymbol{\tau}_{FF}$ represents the feedforward terms and $\boldsymbol{\tau}_{FB}$ represents the feedback terms

$$\boldsymbol{\tau}_{FF} = \mathbf{M}\dot{\boldsymbol{\alpha}} + \mathbf{C}\boldsymbol{\nu} + \mathbf{D}\boldsymbol{\nu} \tag{20}$$

$$\boldsymbol{\tau}_{FB} = -\mathbf{\Gamma}_2\mathbf{z}_2 \tag{21}$$

with $\mathbf{\Gamma}_2 > 0$, which results in

$$\dot{V}_2 = -\mathbf{z}_2^\top \mathbf{\Gamma}_2 \mathbf{z}_2 < 0, \tag{22}$$

which makes the origin of the $\mathbf{z}_2$-dynamics

$$\dot{\mathbf{z}}_2 = -\mathbf{M}^{-1}\mathbf{\Gamma}_2\mathbf{z}_2 \tag{23}$$

UGES.

Remark 1: It is also possible to choose $\boldsymbol{\tau}$ in (19) as

$$\boldsymbol{\tau} = \mathbf{M}\dot{\boldsymbol{\alpha}} + \mathbf{C}\boldsymbol{\alpha} + \mathbf{D}\boldsymbol{\alpha} - \mathbf{\Gamma}_2\mathbf{z}_2, \tag{24}$$

which changes (23) to

$$\dot{\mathbf{z}}_2 = -\mathbf{M}^{-1}(\mathbf{C} + \mathbf{D} + \mathbf{\Gamma}_2)\mathbf{z}_2, \tag{25}$$

where the convergence rate of the $\mathbf{z}_2$-dynamics now becomes influenced by the ship's $\mathbf{C}$ and $\mathbf{D}$ matrices. However, since $\dot{V}_2 = -\mathbf{z}_2{}^\top(\Gamma_2 + \mathbf{D})\,\mathbf{z}_2 \leq -\mathbf{z}_2{}^\top\Gamma_2\mathbf{z}_2$, the convergence rate is no worse than what is achieved by (19).

The total closed-loop dynamics based on (19) become

$$\begin{aligned} \dot{\mathbf{z}}_1 &= \mathbf{S}^\top\mathbf{z}_1 - \mathbf{\Gamma}_1\mathbf{z}_1 + \mathbf{z}_2 && (26) \\ \dot{\mathbf{z}}_2 &= -\mathbf{M}^{-1}\mathbf{\Gamma}_2\mathbf{z}_2. && (27) \end{aligned}$$

Theorem 1: The origin $(\mathbf{z}_1, \mathbf{z}_2) = (\mathbf{0}, \mathbf{0})$ of the overall system (26)-(27) is UGES.

Proof: As shown earlier, the two subsystems (26) and (27) are separately UGES. Additionally, since the interconnection term $\mathbf{z}_2$ enters linearly in (26), all the necessary conditions for UGES of the cascaded system are met according to Proposition 2.3 in [17]. ■

Note that the above UGES result is based on the assumption that unbounded control input is available, due to the

choice of (11) and (21). However, this is not physically possible to achieve since the saturation constraints of the actuators limit the achievable control input. In the following sections, we introduce nonlinear feedback terms which are bounded.

B. NONLINEAR POSE FEEDBACK AND LINEAR VELOCITY FEEDBACK (NP-LV)

We now introduce nonlinear pose feedback, inspired by the constant bearing (CB) guidance concept, which was originally used for ship control in [7]. CB guidance is a so-called two-point guidance scheme developed for interceptor missiles, where the interceptor is supposed to align the relative interceptor-target velocity along the line-of-sight (LOS) vector between the interceptor and the target. The most common method of implementing CB guidance is to make the rotation rate of the interceptor velocity directly proportional to the rotation rate of the interceptor-target LOS, which is widely known as proportional navigation. However, CB guidance can also be implemented through the direct velocity assignment

$$\mathbf{v}_d = \mathbf{v}_t - U_{a,max}\frac{\tilde{\mathbf{p}}}{\sqrt{\tilde{\mathbf{p}}^\top\tilde{\mathbf{p}} + \Delta_p^2}}, \tag{28}$$

where $\mathbf{v}_t \in \mathbb{R}^2$ is a target velocity, and

$$\tilde{\mathbf{p}} \triangleq \mathbf{p} - \mathbf{p}_t \tag{29}$$

is the LOS vector from the target position $\mathbf{p}_t = [x_t, y_t]^\top \in \mathbb{R}^2$ to the interceptor position $\mathbf{p} = [x, y]^\top \in \mathbb{R}^2$. Additionally, $U_{a,max} > 0$ represents the maximum approach speed toward the target, and $\Delta_{\tilde{p}} > 0$ is a tuning parameter that affects the transient convergence behavior between the interceptor and the target. The direct velocity assignment (28) can be seen as a CB guidance approach since in addition to assigning the target speed, a relative approach velocity is assigned along the interceptor-target LOS vector $\tilde{\mathbf{p}}$ to ensure a smooth rendezvous. This relative approach velocity is bounded by $U_{a,max}$ for large $\tilde{\mathbf{p}}$ relative to Δ_p. The result of using such nonlinear feedback is shown for a scalar error $e \in \mathbb{R}$ in Fig. 2, where the effect of varying Δ gains are shown. The linear and nonlinear functions displayed in Fig. 2 are respectively given as $\sigma(e) = \kappa e$ (LF) and $\sigma(e) = \kappa\frac{e}{\sqrt{e^2+\Delta^2}}$ (NF), where $\kappa = 6$.

By introducing nonlinear feedback to the pose control part, the stabilising function is now chosen as

$$\boldsymbol{\alpha} = \mathbf{R}^\top\dot{\boldsymbol{\eta}}_t - \mathbf{K}_1(\mathbf{z}_1)\mathbf{z}_1, \tag{30}$$

where

$$\mathbf{K}_1(\mathbf{z}_1) \triangleq \boldsymbol{\Gamma}_1\boldsymbol{\Omega}(\mathbf{z}_1), \tag{31}$$

and

$$\boldsymbol{\Omega}(\mathbf{z}_1) \triangleq \begin{bmatrix} \frac{1}{\sqrt{\mathbf{z}_{1,\tilde{p}}^\top\mathbf{z}_{1,\tilde{p}} + \Delta_p^2}}\mathbf{I}_{2\times2} & \mathbf{0}_{2\times1} \\ \mathbf{0}_{1\times2} & \frac{1}{\sqrt{z_{1,\tilde{\psi}}^2 + \Delta_\psi^2}} \end{bmatrix} \tag{32}$$

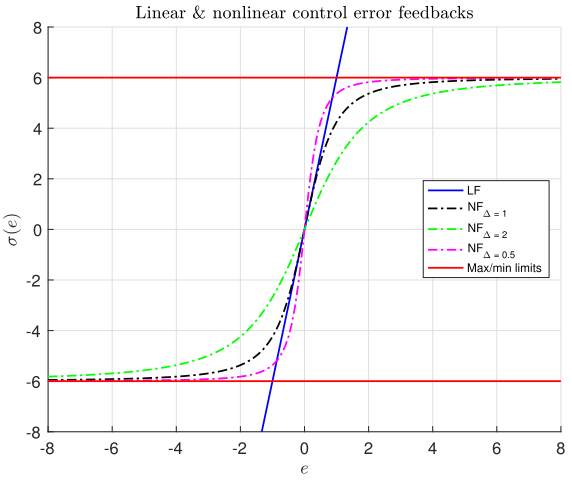

FIGURE 2. The abbreviation LF represents a linear feedback term as a function of the control error e, while NF represents a nonlinear feedback term based on a sigmoid function of e with a tuning parameter Δ, such as in (28).

with $\boldsymbol{\Gamma}_1 > 0$ as before, $\mathbf{z}_{1,\tilde{p}} \triangleq [z_{1,1}, z_{1,2}]^\top$, $z_{1,\tilde{\psi}} \triangleq z_{1,3}$, $\Delta_p > 0$ and $\Delta_\psi > 0$. It is also possible to choose

$$\boldsymbol{\Omega}(\mathbf{z}_1) = \frac{1}{\sqrt{\mathbf{z}_1^\top\mathbf{z}_1 + \Delta^2}}\mathbf{I}_{3\times3}, \tag{33}$$

if $\Delta_p = \Delta_\psi = \Delta > 0$, but then it is not possible to define a different transient behavior for the position and heading.

Choosing (32) leads to

$$\dot{V}_1 = -\mathbf{z}_1^\top\mathbf{K}_1(\mathbf{z}_1)\mathbf{z}_1 + \mathbf{z}_1^\top\mathbf{z}_2, \tag{34}$$

and

$$\dot{\boldsymbol{\alpha}} = \mathbf{R}^\top\ddot{\boldsymbol{\eta}}_t + \mathbf{S}^\top\mathbf{R}^\top\dot{\boldsymbol{\eta}}_t - \dot{\mathbf{K}}_1(\mathbf{z}_1)\mathbf{z}_1 - \mathbf{K}_1(\mathbf{z}_1)\dot{\mathbf{z}}_1, \tag{35}$$

where

$$\dot{\mathbf{K}}_1(\mathbf{z}_1) = -\boldsymbol{\Gamma}_1\begin{bmatrix} \frac{\mathbf{z}_{1,\tilde{p}}^\top\dot{\mathbf{z}}_{1,\tilde{p}}\mathbf{I}_{2\times2}}{(\mathbf{z}_{1,\tilde{p}}^\top\mathbf{z}_{1,\tilde{p}} + \Delta_p^2)^{\frac{3}{2}}} & \mathbf{0}_{2\times1} \\ \mathbf{0}_{1\times2} & \frac{z_{1,\tilde{\psi}}\dot{z}_{1,\tilde{\psi}}}{(z_{1,\tilde{\psi}}^2 + \Delta_\psi^2)^{\frac{3}{2}}} \end{bmatrix}. \tag{36}$$

The total closed-loop dynamics now changes from (26)-(27) to

$$\dot{\mathbf{z}}_1 = \mathbf{S}^\top\mathbf{z}_1 - \mathbf{K}_1(\mathbf{z}_1)\mathbf{z}_1 + \mathbf{z}_2 \tag{37}$$

$$\dot{\mathbf{z}}_2 = -\mathbf{M}^{-1}\boldsymbol{\Gamma}_2\mathbf{z}_2. \tag{38}$$

Here, we notice that when the control error is large, i.e., when

$$|\mathbf{z}_1| \gg 1 \Rightarrow \dot{\mathbf{z}}_1 \approx \mathbf{S}^\top\mathbf{z}_1 - \boldsymbol{\Gamma}_1\boldsymbol{\rho}(\mathbf{z}_1) + \mathbf{z}_2, \tag{39}$$

where $\boldsymbol{\rho}(\mathbf{z}_1) = \text{col}(\mathbf{z}_{1,\tilde{p}}/|\mathbf{z}_{1,\tilde{p}}|, \mathbf{z}_{1,\tilde{\psi}}/|\mathbf{z}_{1,\tilde{\psi}}|)$ is a vectorial sign-like function that saturates the error $\mathbf{z}_1$. Additionally, when the control error is small, i.e., when

$$|\mathbf{z}_1| \approx 0 \Rightarrow \dot{\mathbf{z}}_1 = \mathbf{S}^\top\mathbf{z}_1 - \boldsymbol{\Gamma}_1\begin{bmatrix} \frac{1}{\Delta_p}\mathbf{I}_{2\times2} & \mathbf{0}_{2\times1} \\ \mathbf{0}_{1\times2} & \frac{1}{\Delta_\psi} \end{bmatrix}\mathbf{z}_1 + \mathbf{z}_2, \tag{40}$$

where the linear dynamics is recovered, scaled by Δ_p and Δ_ψ, around the origin. It should be noted that $\boldsymbol{\rho}(\mathbf{z}_1)$ only saturates the $\mathbf{z}_1$ error dynamics and does not have a direct relationship with the actuator saturation level.

Theorem 2: The origin $(\mathbf{z}_1, \mathbf{z}_2) = (\mathbf{0}, \mathbf{0})$ is uniformly globally asymptotically stable (UGAS), and on each compact set $B \subset \mathbb{R}^6$ containing the origin, it is uniformly exponentially stable (UES).

Proof: We have that the $\mathbf{z}_2$-dynamics is UGES, the unperturbed $\mathbf{z}_1$-dynamics is UGAS, since (6) is $\mathcal{C}^1$ and positive definite, $\dot{V}_1$ is negative definite $\forall \mathbf{z}_1 \neq \mathbf{0}$ and (6) is radially unbounded $\forall \mathbf{z}_1 \neq \mathbf{0}$.

Next, it can be shown that the $\mathbf{z}_1$-subsystem is growth restricted by satisfying Assumption 7 in [17], where $\alpha_4(s) = s$, $\alpha_5(s) = 1$, $\alpha_1(s) = \frac{1}{2}s^2$ and $\alpha_6(s) = \sqrt{2s}$. Additionally, Assumption 8 in [17] is satisfied by having $\lambda = 2$, $V = \frac{1}{2}\mathbf{z}_1^\top \mathbf{z}_1$ and $W_1(\mathbf{z}_1) = \mathbf{z}_1^\top \mathbf{K}_1(\mathbf{z}_1)\mathbf{z}_1$. With these conditions satisfied, Theorem 2.3 in [17] states that the origin $(\mathbf{z}_1, \mathbf{z}_2) = (\mathbf{0}, \mathbf{0})$ is UGAS.

For $|\mathbf{z}(t_0)| \in B$ and the definition of UGAS, there exists $L > 0$ so that $|\mathbf{z}(t)| \leq L$, $\forall t \geq t_0 \geq 0$. This also means that $\left|\mathbf{z}_{1,\tilde{p}}\right| \leq L$ and $\left|\mathbf{z}_{1,\tilde{\psi}}\right| \leq L$, which further implies $\exists \gamma > 0$ such that $\boldsymbol{\Gamma}_1 \boldsymbol{\Omega}(\mathbf{z}_1) + \boldsymbol{\Omega}(\mathbf{z}_1)\boldsymbol{\Gamma}_1 > \gamma \mathbf{I}$. Using the quadratic Lyapunov function

$$V(\mathbf{z}_1, \mathbf{z}_2) = \mathbf{z}_1^\top \mathbf{z}_1 + \frac{1}{2} b_2 \mathbf{z}_2^\top \mathbf{M} \mathbf{z}_2, \tag{41}$$

where $b_2 > 0$, we get

$$\begin{aligned}
\dot{V} &= 2\mathbf{z}_1^\top \left[-\mathbf{S}\mathbf{z}_1 - \boldsymbol{\Gamma}_1 \boldsymbol{\Omega}(\mathbf{z}_1)\mathbf{z}_1 + \mathbf{z}_2\right] \\
&\quad + b_2 \mathbf{z}_2^\top \mathbf{M} \left[-\mathbf{M}^{-1} \boldsymbol{\Gamma}_2 \mathbf{z}_2\right] && (42) \\
&= -\mathbf{z}_1^\top \left[\boldsymbol{\Gamma}_1 \boldsymbol{\Omega}(\mathbf{z}_1) + \boldsymbol{\Omega}(\mathbf{z}_1)\boldsymbol{\Gamma}_1\right] \mathbf{z}_1 + 2\mathbf{z}_1^\top \mathbf{z}_2 \\
&\quad - b_2 \mathbf{z}_2^\top \boldsymbol{\Gamma}_2 \mathbf{z}_2 && (43) \\
&\leq -\gamma \left|\mathbf{z}_1\right|^2 + 2\left|\mathbf{z}_1\right| \left|\mathbf{z}_2\right| - b_2 \lambda_{\min}\left(\boldsymbol{\Gamma}_2\right) \left|\mathbf{z}_2\right|^2 && (44) \\
&= -\frac{\gamma}{2}\left|\mathbf{z}_1\right|^2 - \frac{\gamma}{2}\left|\mathbf{z}_1\right|^2 + \kappa \left|\mathbf{z}_1\right|^2 + \frac{1}{\kappa}\left|\mathbf{z}_2\right|^2 \\
&\quad - b_2 \lambda_{\min}\left(\boldsymbol{\Gamma}_2\right) \left|\mathbf{z}_2\right|^2 && (45) \\
&= -\frac{\gamma}{2}\left|\mathbf{z}_1\right|^2 - \left(b_2 \lambda_{\min}\left(\boldsymbol{\Gamma}_2\right) - \frac{2}{\gamma}\right) \left|\mathbf{z}_2\right|^2, && (46)
\end{aligned}$$

where we used Young's inequality $xy \leq \kappa x^2 + \frac{1}{4\kappa} y^2$, $\kappa = \frac{\gamma}{2} > 0$. Choosing for instance

$$b_2 = \frac{1}{\lambda_{\min}\left(\boldsymbol{\Gamma}_2\right)} \left(\frac{\gamma}{2} + \frac{2}{\gamma}\right), \tag{47}$$

gives

$$\dot{V} \leq -\frac{\gamma}{2}\left|\mathbf{z}\right|^2, \tag{48}$$

which proves UES on the compact set B. ∎

Remark 2: UGAS shows that stability of this system is global. The second part of the theorem shows that for any practical set B of initial conditions, the convergence is in fact exponential.

C. NONLINEAR POSE AND VELOCITY FEEDBACKS (NP-NV)

We now also introduce nonlinear velocity feedback, which changes the control law (19) to

$$\boldsymbol{\tau} = \mathbf{M}\dot{\boldsymbol{\alpha}} + \mathbf{C}\boldsymbol{\nu} + \mathbf{D}\boldsymbol{\nu} - \mathbf{K}_2(\mathbf{z}_2)\mathbf{z}_2, \tag{49}$$

where

$$\mathbf{K}_2(\mathbf{z}_2) = \boldsymbol{\Gamma}_2 \begin{bmatrix} \frac{1}{\sqrt{\mathbf{z}_{2,\tilde{\nu}}^\top \mathbf{z}_{2,\tilde{\nu}} + \Delta_\nu^2}} \mathbf{I}_{2\times 2} & \mathbf{0}_{2\times 1} \\ \mathbf{0}_{1\times 2} & \frac{1}{\sqrt{z_{2,\tilde{r}}^2 + \Delta_r^2}} \end{bmatrix} \tag{50}$$

with $\boldsymbol{\Gamma}_2 > 0$ as before, $\mathbf{z}_{2,\tilde{\nu}} \triangleq [z_{2,1}, z_{2,2}]^\top$, $z_{2,\tilde{r}} \triangleq z_{2,3}$, $\Delta_\nu > 0$ and $\Delta_r > 0$. In this case, the derivative of V_2 becomes

$$\dot{V}_2 = -\mathbf{z}_2^\top \mathbf{K}_2(\mathbf{z}_2)\mathbf{z}_2, \tag{51}$$

and the total closed-loop dynamics become

$$\dot{\mathbf{z}}_1 = \mathbf{S}^\top \mathbf{z}_1 - \mathbf{K}_1(\mathbf{z}_1)\mathbf{z}_1 + \mathbf{z}_2 \tag{52}$$

$$\dot{\mathbf{z}}_2 = -\mathbf{M}^{-1}\mathbf{K}_2(\mathbf{z}_2)\mathbf{z}_2. \tag{53}$$

Theorem 3: The origin $(\mathbf{z}_1, \mathbf{z}_2) = (\mathbf{0}, \mathbf{0})$ is UGAS, and on each compact set $B \subset \mathbb{R}^6$ containing the origin, it is UES.

Proof: The $\mathbf{z}_2$-dynamics can be proven to be UGAS using Theorem 4.9 in [18], since (16) is $\mathcal{C}^1$ and positive definite, $\dot{V}_2$ is negative definite $\forall \mathbf{z}_2 \neq \mathbf{0}$ and (16) is radially unbounded $\forall \mathbf{z}_2 \neq \mathbf{0}$. A similar conclusion can be made for the unperturbed $\mathbf{z}_1$-dynamics, as shown in Theorem 3.

Next, it can be shown that the $\mathbf{z}_1$-subsystem is growth restricted by satisfying Assumption 7 in [17], where $\alpha_4(s) = s$, $\alpha_5(s) = 1$, $\alpha_1(s) = \frac{1}{2}s^2$ and $\alpha_6(s) = \sqrt{2s}$. Additionally, Assumption 8 in [17], is satisfied by having $\lambda = 2$, $V = \frac{1}{2}\mathbf{z}_1^\top \mathbf{z}_1$ and $W_1(\mathbf{z}_1) = \mathbf{z}_1^\top \mathbf{K}_1(\mathbf{z}_1)\mathbf{z}_1$. With these conditions satisfied, Theorem 2.3 in [17] states that the origin $(\mathbf{z}_1, \mathbf{z}_2) = (\mathbf{0}, \mathbf{0})$ is UGAS.

For $|\mathbf{z}(t_0)| \in B$ and the definition of UGAS, there exists $L > 0$ so that $|\mathbf{z}(t)| \leq L$, $\forall t \geq t_0 \geq 0$. This also means that $\left|\mathbf{z}_{1,p}\right| \leq L$, $\left|\mathbf{z}_{1,\psi}\right| \leq L$, $\left|\mathbf{z}_{2,v}\right| \leq L$ and $\left|\mathbf{z}_{2,r}\right| \leq L$, which further implies $\exists \gamma_i > 0$ such that $\boldsymbol{\Gamma}_i \boldsymbol{\Omega}(\mathbf{z}_i) + \boldsymbol{\Omega}(\mathbf{z}_i)\boldsymbol{\Gamma}_i > \gamma_i \mathbf{I}$, $i = 1, 2$. Using the quadratic Lyapunov function

$$V(\mathbf{z}_1, \mathbf{z}_2) = \mathbf{z}_1^\top \mathbf{z}_1 + b_2 \mathbf{z}_2^\top \mathbf{M} \mathbf{z}_2 \tag{54}$$

where $b_2 > 0$, we get

$$\begin{aligned}
\dot{V} &= 2\mathbf{z}_1^\top \left[-\mathbf{S}\mathbf{z}_1 - \boldsymbol{\Gamma}_1 \boldsymbol{\Omega}(\mathbf{z}_1)\mathbf{z}_1 + \mathbf{z}_2\right] \\
&\quad + 2b_2 \mathbf{z}_2^\top \mathbf{M} \left[-\mathbf{M}^{-1} \boldsymbol{\Gamma}_2 \boldsymbol{\Omega}(\mathbf{z}_2)\mathbf{z}_2\right] && (55) \\
&= -\mathbf{z}_1^\top \left[\boldsymbol{\Gamma}_1 \boldsymbol{\Omega}(\mathbf{z}_1) + \boldsymbol{\Omega}(\mathbf{z}_1)\boldsymbol{\Gamma}_1\right] \mathbf{z}_1 + 2\mathbf{z}_1^\top \mathbf{z}_2 \\
&\quad - b_2 \mathbf{z}_2^\top \left[\boldsymbol{\Gamma}_2 \boldsymbol{\Omega}(\mathbf{z}_2) + \boldsymbol{\Omega}(\mathbf{z}_2)\boldsymbol{\Gamma}_2\right] \mathbf{z}_2 && (56) \\
&\leq -\gamma_1 \left|\mathbf{z}_1\right|^2 + 2\left|\mathbf{z}_1\right| \left|\mathbf{z}_2\right| - b_2 \gamma_2 \left|\mathbf{z}_2\right|^2 && (57) \\
&= -\frac{\gamma_1}{2}\left|\mathbf{z}_1\right|^2 - \frac{\gamma_1}{2}\left|\mathbf{z}_1\right|^2 + \kappa \left|\mathbf{z}_1\right|^2 + \frac{1}{\kappa}\left|\mathbf{z}_2\right|^2 \\
&\quad - b_2 \gamma_2 \left|\mathbf{z}_2\right|^2 && (58) \\
&= -\frac{\gamma_1}{2}\left|\mathbf{z}_1\right|^2 - \left(b_2 \gamma_2 - \frac{2}{\gamma_1}\right) \left|\mathbf{z}_2\right|^2, && (59)
\end{aligned}$$

where we used Young's inequality. Choosing for instance

$$b_2 = \frac{1}{\gamma_2}\left(\frac{\gamma_1}{2} + \frac{2}{\gamma_1}\right) \tag{60}$$

gives

$$\dot{V} \leq -\frac{\gamma_1}{2}|\mathbf{z}|^2, \tag{61}$$

which proves UES on the compact set B. ■

IV. SUGGESTED TUNING RULES

Considering the $\mathbf{z}_1$-dynamics in (26), (37), and (52), it can be seen that the choice of the $\mathbf{\Gamma}_1$ gain matrix determines the time constants of the $\mathbf{z}_1$-dynamics with linear feedback only. Hence, a time-constant matrix for the kinematic subsystem can be used to define the linear gain matrix as

$$\mathbf{\Gamma}_1 \triangleq \mathbf{T}_1^{-1} \tag{62}$$

where

$$\mathbf{T}_1 = \begin{bmatrix} T_p & 0 & 0 \\ 0 & T_p & 0 \\ 0 & 0 & T_\psi \end{bmatrix}, \tag{63}$$

with $T_p > 0$ and $T_\psi > 0$ being the time constants for position control and heading control, respectively.

A similar observation can be made for the $\mathbf{z}_2$-dynamics in (27), (38), and (53), where the choice of the $\mathbf{\Gamma}_2$ gain matrix determines the time constants of the $\mathbf{z}_2$-dynamics with linear feedback only. Similarly, we can define the choice of linear gain matrix for the kinetic subsystem based on a time-constant matrix as

$$\mathbf{\Gamma}_2 \triangleq \mathbf{M}\mathbf{T}_2^{-1}, \tag{64}$$

where

$$\mathbf{T}_2 = \begin{bmatrix} T_v & 0 & 0 \\ 0 & T_v & 0 \\ 0 & 0 & T_r \end{bmatrix},$$

with $T_v > 0$ and $T_r > 0$ are the time constants for linear velocity control and yaw rate control, respectively.

It is favorable for the kinetic subsystem to have faster dynamics than the kinematic subsystem. Hence, the kinetic dynamics must have smaller time constants, that is

$$T_v < T_p \tag{65}$$

$$T_r < T_\psi. \tag{66}$$

Also, Δ_p, Δ_ψ, Δ_v and Δ_r must be chosen. The control parameter Δ is usually known as the lookahead distance in line of sight guidance [9]. In [19], it is shown that a small Δ-value corresponds to fast convergence to the path, but with a large overshoot, while a large Δ-value reduces overshoot and results in smooth but slow convergence. Here, the Δ-values scale the linear feedback gains and therefore the time constants of the linear region around the origin. If the Δ-values are equal to 1, they will result in the same response as the linear controllers in the linear region. But if they are larger than 1, they will give a slower response in this region. If they are chosen to be smaller than 1, they will give a faster response. Hence, the Δ-values for the NP and NV feedback terms must be chosen such that the conditions in (65)-(66) are still satisfied in the linear region, where the time constants will be related to $\mathbf{\Gamma}_1(1,1)/\Delta_p$, $\mathbf{\Gamma}_1(3,3)/\Delta_\psi$, $\mathbf{\Gamma}_2(1,1)/\Delta_v$, and $\mathbf{\Gamma}_2(3,3)/\Delta_r$.

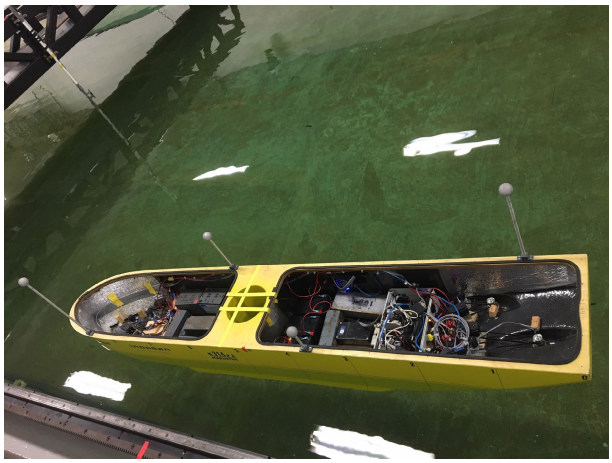

FIGURE 3. C/S inocean cat I arctic drillship in the marine cybernetics laboratory at NTNU.

V. SIMULATION AND EXPERIMENTAL RESULTS

A. SHIP MODEL

The model-scale cybership *C/S Inocean Cat I Arctic Drillship* (CSAD), with parameters from [20], is used to test the performance of the proposed motion controllers through both simulations and experiments. CSAD is a 1:90 scale replica of the full-scale Equinor Cat I Drillship, with a length of $L = 2.578$ (m), shown in Fig 3. The ship is fully actuated with six azimuth thrusters.

B. PERFORMANCE METRICS

To evaluate and compare the performance of the different controllers, some suitable performance metrics must be used. We define

$$e(t) \triangleq \sqrt{\tilde{\boldsymbol{\eta}}(t)^\top \tilde{\boldsymbol{\eta}}(t)}, \tag{67}$$

as the error input to be used in the performance metrics, with $\tilde{\boldsymbol{\eta}} = [\tilde{x}, \tilde{y}, \tilde{\psi}]^\top \triangleq \boldsymbol{\eta} - \boldsymbol{\eta}_t$. Here, since the position and yaw angle have different units, we define the normalized signals $\tilde{x}$, $\tilde{y}$, and $\tilde{\psi}$ in the intervals $[-0.5, 0.5]$ in the expected operational space of the ship [21]. To obtain this normalization, the position errors are divided by 4 (m) and the yaw error is divided by $\frac{\pi}{2}$ (rad), since the position errors will be in the intervals $[-2, 2]$ (m) and the yaw error will be in the interval $[-\frac{\pi}{4}, \frac{\pi}{4}]$ (rad). In addition, these signals represent the instantaneous control errors, while we would like to consider the accumulated errors over time. Hence, we use the performance metric IAE (integral of the absolute

error)

$$IAE(t) \triangleq \int_0^t |e(\tau)| d\tau, \tag{68}$$

which integrates the temporal evolution of the absolute value of the error without adding any weight to the error. We will also use the so-called IAEW metric, which scales the IAE metric by the energy consumption, and which was proposed in [15]. Specifically, the IAEW can be computed as

$$IAEW(t) \triangleq \int_0^t |e(\tau)| d\tau \int_0^t P(\tau) d\tau, \tag{69}$$

where

$$P(t) = |\boldsymbol{\nu}(t)^\top \boldsymbol{\tau}(t)| \tag{70}$$

represents the mechanical power of the ship. IAEW thus indicates which controller has the best combined control accuracy and energy use in one single metric. Normally, the sum of the weighted square of the state and control input is integrated as a cost function to find optimal control values. We have, on the other hand, chosen performance metrics as multiplication of sub-objectives in order to avoid mixed units in a sum of physical quantities.

C. TEST SETUP AND CONTROLLER TUNING

Since this article concerns the comparison of combinations of feedback terms, we have chosen to use a so-called 4-corner test to be able to effectively demonstrate the closed-loop control performance differences. This test is illustrated in Fig. 4, and has e.g. been used in [22] and [11] to evaluate the performance of dynamic positioning control algorithms. Since the test consists of a set of setpoint-change maneuvers, both moving forwards and backwards, the feedforward terms associated with the $\mathbf{C}(\boldsymbol{\nu})$ and $\mathbf{D}(\boldsymbol{\nu})$ matrices are removed from the control laws. This removal also serves to better illustrate the main differences between the considered feedback control combinations.

In particular, the 4-corner test is performed as follows: The ship is first initialized to point straight North, at heading 0 (*deg*). Then the following setpoint changes are executed:

1) Position change 2 (*m*) straight North: Tests a pure surge movement ahead.
2) Position change 2 (*m*) straight East: Tests a pure sway movement in the starboard direction.
3) Heading change 45 (*deg*) clockwise: Tests a pure yaw motion while keeping position steady.
4) Position change 2 (*m*) straight South: Tests a combined surge-sway movement while keeping the heading steady.
5) Position change 2 (*m*) straight West and heading change 45 (*deg*) counterclockwise: Tests a combined surge-sway-yaw movement.

Through these setpoint changes, this test simplifies the control problem down to three 1-DOF motions in surge, sway, and yaw, respectively. The final two setpoint changes represent 2-DOFs and 3-DOFs coupled motions. The system is implemented such that the target will automatically change setpoint when the ship is within 0.003 (*m*) from the target in both x and y direction and 0.2 (*deg*) from the target heading. When the 4-corner test is completed, the ship will have returned to its initial position and heading, ready for a new test run from the same pose and along the same track.

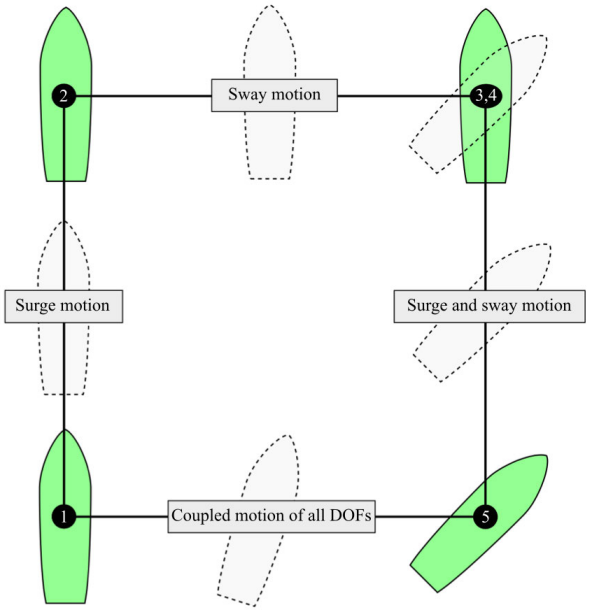

FIGURE 4. The 4-corner test. Modified from [22].

Hence, the control laws used in the test are simplified to their feedback essence as follows.

LP-LV:

$$\boldsymbol{\alpha} = -\boldsymbol{\Gamma}_1 \mathbf{z}_1 \tag{71a}$$
$$\dot{\boldsymbol{\alpha}} = -\boldsymbol{\Gamma}_1 \dot{\mathbf{z}}_1 \tag{71b}$$
$$\boldsymbol{\tau} = \mathbf{M}\dot{\boldsymbol{\alpha}} - \boldsymbol{\Gamma}_2 \mathbf{z}_2, \tag{71c}$$

The control gains have been chosen such that the LP-LV control input stays within the magnitude saturations of the actuators. This has lead us to the gains $\boldsymbol{\Gamma}_1 = diag([0.08, 0.08, 0.0698])$ and $\boldsymbol{\Gamma}_2 = diag([0.2, 0.2, 0.1745])\mathbf{M}$. Using (62) and (64), we get the following corresponding time-constant matrices:

$$\mathbf{T}_1 = \begin{bmatrix} T_p & 0 & 0 \\ 0 & T_p & 0 \\ 0 & 0 & T_\psi \end{bmatrix} = \boldsymbol{\Gamma}_1^{-1} = \begin{bmatrix} 12.5 & 0 & 0 \\ 0 & 12.5 & 0 \\ 0 & 0 & 14.32 \end{bmatrix} \tag{72}$$

and

$$\mathbf{T}_2 = \begin{bmatrix} T_v & 0 & 0 \\ 0 & T_v & 0 \\ 0 & 0 & T_r \end{bmatrix} = \mathbf{M}^{-1}\boldsymbol{\Gamma}_2^{-1}$$

$$= \begin{bmatrix} 5 & 0 & 0 \\ 0 & 5 & 0 \\ 0 & 0 & 5.73 \end{bmatrix}. \tag{73}$$

The corresponding LP-LV time constants for the kinematic and kinetic controllers are thus $T_p = 12.5 > T_v = 5$ and $T_\psi = 14.32 > T_r = 5.73$, which satisfy the tuning rules.

NP-LV:

$$\boldsymbol{\alpha} = -\mathbf{K}_1(\mathbf{z}_1)\mathbf{z}_1 \tag{74a}$$
$$\dot{\boldsymbol{\alpha}} = -\dot{\mathbf{K}}_1(\mathbf{z}_1)\mathbf{z}_1 - \mathbf{K}_1(\mathbf{z}_1)\dot{\mathbf{z}}_1 \tag{74b}$$
$$\boldsymbol{\tau} = \mathbf{M}\dot{\boldsymbol{\alpha}} - \boldsymbol{\Gamma}_2\mathbf{z}_2, \tag{74c}$$

Here, we reuse the gains found for the LP-LV controller in order to be able to clearly see the effects of introducing the delta-parameters on the performance. Also, Δ_p and Δ_ψ are chosen so that the time constants associated with the kinematic control loop do not become smaller than that of the kinetic control loop. We have therefore chosen $\Delta_p = 0.5$ and $\Delta_\psi = 0.5$. This gives us the following corresponding time-constant matrices:

$$\mathbf{T}_1 = \begin{bmatrix} T_p & 0 & 0 \\ 0 & T_p & 0 \\ 0 & 0 & T_\psi \end{bmatrix} = \left(\boldsymbol{\Gamma}_1 \begin{bmatrix} \frac{1}{\Delta_p} & 0 & 0 \\ 0 & \frac{1}{\Delta_p} & 0 \\ 0 & 0 & \frac{1}{\Delta_\psi} \end{bmatrix} \right)^{-1}$$
$$= \begin{bmatrix} 12.5 * 0.5 & 0 & 0 \\ 0 & 12.5 * 0.5 & 0 \\ 0 & 0 & 14.32 * 0.5 \end{bmatrix}$$
$$= \begin{bmatrix} 6.25 & 0 & 0 \\ 0 & 6.25 & 0 \\ 0 & 0 & 7.16 \end{bmatrix} \tag{75}$$

and

$$\mathbf{T}_2 = \begin{bmatrix} 5 & 0 & 0 \\ 0 & 5 & 0 \\ 0 & 0 & 5.73 \end{bmatrix}. \tag{76}$$

With the chosen Δ-values, the time constants in the linear region associated with the NP-LV controller are $T_p = 6.25 > T_v = 5$ and $T_\psi = 7.16 > T_r = 5.73$

NP-NV:

$$\boldsymbol{\alpha} = -\mathbf{K}_1(\mathbf{z}_1)\mathbf{z}_1 \tag{77a}$$
$$\dot{\boldsymbol{\alpha}} = -\dot{\mathbf{K}}_1(\mathbf{z}_1)\mathbf{z}_1 - \mathbf{K}_1(\mathbf{z}_1)\dot{\mathbf{z}}_1 \tag{77b}$$
$$\boldsymbol{\tau} = \mathbf{M}\dot{\boldsymbol{\alpha}} - \mathbf{K}_2(\mathbf{z}_2)\mathbf{z}_2. \tag{77c}$$

Similar to the NP-LV controller, we reuse the gains for the LP-LV controller, and the Δ-values Δ_p, Δ_ψ, Δ_v and Δ_r for the NP-NV controller are chosen such that the time constants associated with the kinematic control loop do not become smaller than that of the kinetic control loop. We have therefore chosen $\Delta_p = 0.5$, $\Delta_\psi = 0.5$, $\Delta_v = 0.7$ and $\Delta_r = 1$. This gives us the following corresponding time-constant matrices:

TABLE 1. Control gains for the 4-corner test.

	LP-LV	NP-LV	NP-NV
$\boldsymbol{\Gamma}_1$	$diag([0.08, 0.08, 0.0698])$	$-\|\|-$	$-\|\|-$
$\boldsymbol{\Gamma}_2$	$diag([0.2, 0.2, 0.1745])\mathbf{M}$	$-\|\|-$	$-\|\|-$
$\Delta_{\tilde{p},\tilde{\psi}}$	-	$[0.5, 0.5]$	$-\|\|-$
$\Delta_{\tilde{v},\tilde{r}}$	-	-	$[0.7, 1]$

matrices:

$$\mathbf{T}_1 = \begin{bmatrix} T_p & 0 & 0 \\ 0 & T_p & 0 \\ 0 & 0 & T_\psi \end{bmatrix}$$
$$= \begin{bmatrix} 12.5 * 0.5 & 0 & 0 \\ 0 & 12.5 * 0.5 & 0 \\ 0 & 0 & 14.32 * 0.5 \end{bmatrix}$$
$$= \begin{bmatrix} 6.25 & 0 & 0 \\ 0 & 6.25 & 0 \\ 0 & 0 & 7.16 \end{bmatrix} \tag{78}$$

and

$$\mathbf{T}_2 = \begin{bmatrix} T_v & 0 & 0 \\ 0 & T_v & 0 \\ 0 & 0 & T_r \end{bmatrix} = \begin{bmatrix} 5 * 0.7 & 0 & 0 \\ 0 & 5 * 0.7 & 0 \\ 0 & 0 & 5.73 * 1 \end{bmatrix}$$
$$= \begin{bmatrix} 3.5 & 0 & 0 \\ 0 & 3.5 & 0 \\ 0 & 0 & 5.73 \end{bmatrix}. \tag{79}$$

With the chosen Δ-values, the time constants in the linear region associated with the NP-NV controller are $T_p = 6.25 > T_v = 3.5$ and $T_\psi = 7.16 > T_r = 5.73$. Finally, the chosen control gains are summarised in Table 1.

D. SIMULATION RESULTS

Since this article focuses on fundamental motion control aspects, it is assumed for simulation purposes that no disturbances and uncertainties are affecting the system. Such disturbances and uncertainties need to be handled with other additional algorithms tailored for the purpose. Also, it is assumed that both the pose vector $\boldsymbol{\eta}$ and velocity vector $\boldsymbol{\nu}$ can be measured.

In Fig. 5-7, the outline of the ship pose is plotted to show the pose motion patterns. Here, the blue outline represents the LP-LV-controlled ship, the dash-dotted black outline represents the NP-LV-controlled ship, the dashed green outline represents the NP-NV-controlled ship, while the red outline represents the 4-corner test box outline. Notice that the vessel has a larger position error when moving from point 5 to point 1, which is natural given that this is the most challenging maneuver to perform, with coupled motion change in all 3-DOFs.

Fig. 8 shows the commanded control inputs for the three controllers. Note that the amount of time each of the controllers use to complete the 4-corner test is different, since the nonlinear feedback controllers modify the convergence

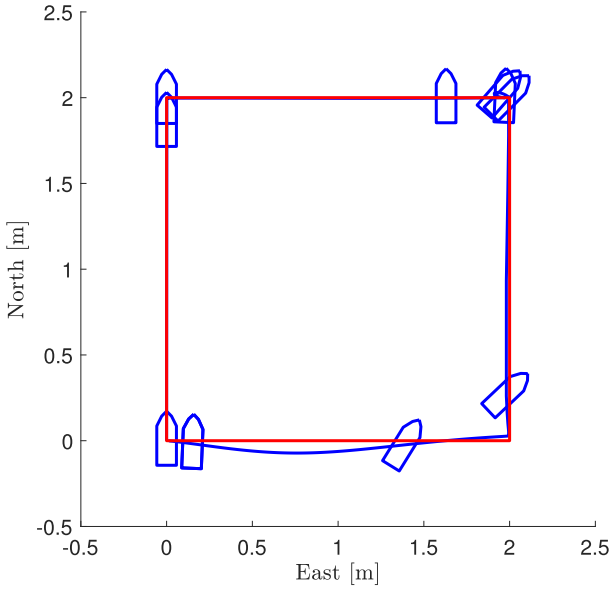

FIGURE 5. The 4-corner simulation: Using LP-LV feedback terms.

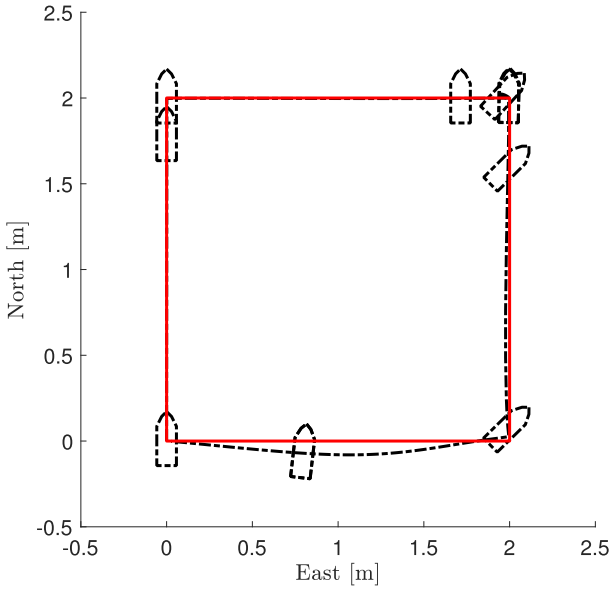

FIGURE 6. The 4-corner simulation: Using NP-LV feedback terms.

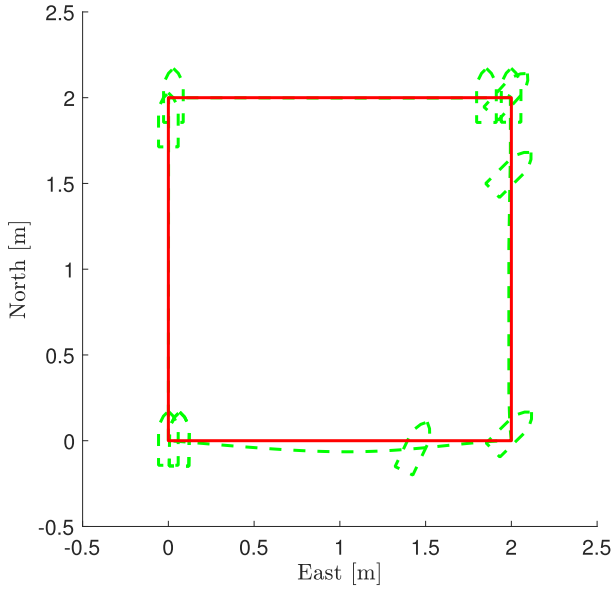

FIGURE 7. The 4-corner simulation: Using NP-NV feedback terms.

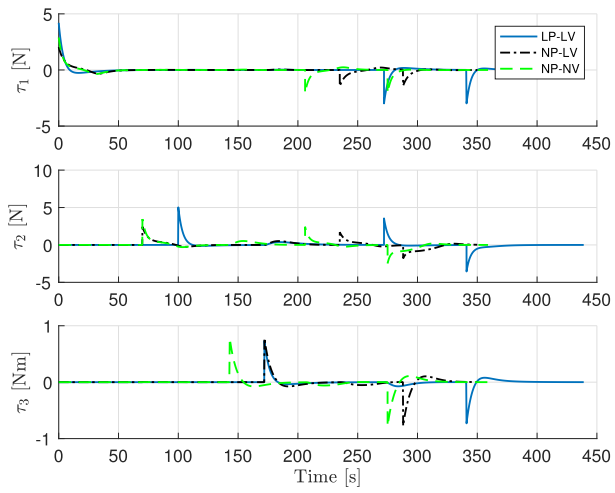

FIGURE 8. The 4-corner simulation: The commanded control inputs.

rate to be faster than the linear feedback controller in the linear regions. Two main results can be seen from Fig. 8. First, the NP-LV controller is the fastest of the three controllers to complete the 4-corner test, followed by the NP-NV and lastly the LP-LV controller. Second, the magnitude of τ_1 and τ_2 are lowest for the NP-LV controller, closely followed by the NP-NV controller. However, τ_3 has the same magnitude for all the considered controllers. Based on this, it can be concluded that the nonlinear position feedback terms of (32) limit the control signal while the nonlinear heading feedback term of (32) does not.

Fig. 9 illustrates how the contribution of the kinematic feedback terms in $\boldsymbol{\alpha}$ are dependent on the error $\mathbf{z}_1$ for the three controllers. In [23], it is shown that the maximum velocities of CSAD are 0.4142 [m/s], 0.109 [m/s] and 6.327 [deg/s] in surge, sway and yaw, respectively. These velocity boundaries are illustrated in Fig. 9, for the plots where the feedback terms get close to or exceed these boundaries. Keep in mind that the velocity terms α_1, α_2, and α_3 are components of the so-called stabilizing function $\boldsymbol{\alpha} = [\alpha_1, \alpha_2, \alpha_2]^\top$. Specifically, it can be seen that α_1 and α_2 are limited for the controllers with a nonlinear feedback term, while the one which has a linear feedback term evolves linearly without any bounds. It is also noticed that there are two different curves for both the NP-LP and NP-NV controllers, which is due to the construction of the denominator in (32) for the position feedback terms. Since the denominator of these feedback terms is both dependent on the error in $z_{1,1}$ and $z_{1,2}$, it is natural that the curves are lower for the setpoint changes associated with 4) and 5) than 1) and 2) from Fig. 4. It should also be noted that

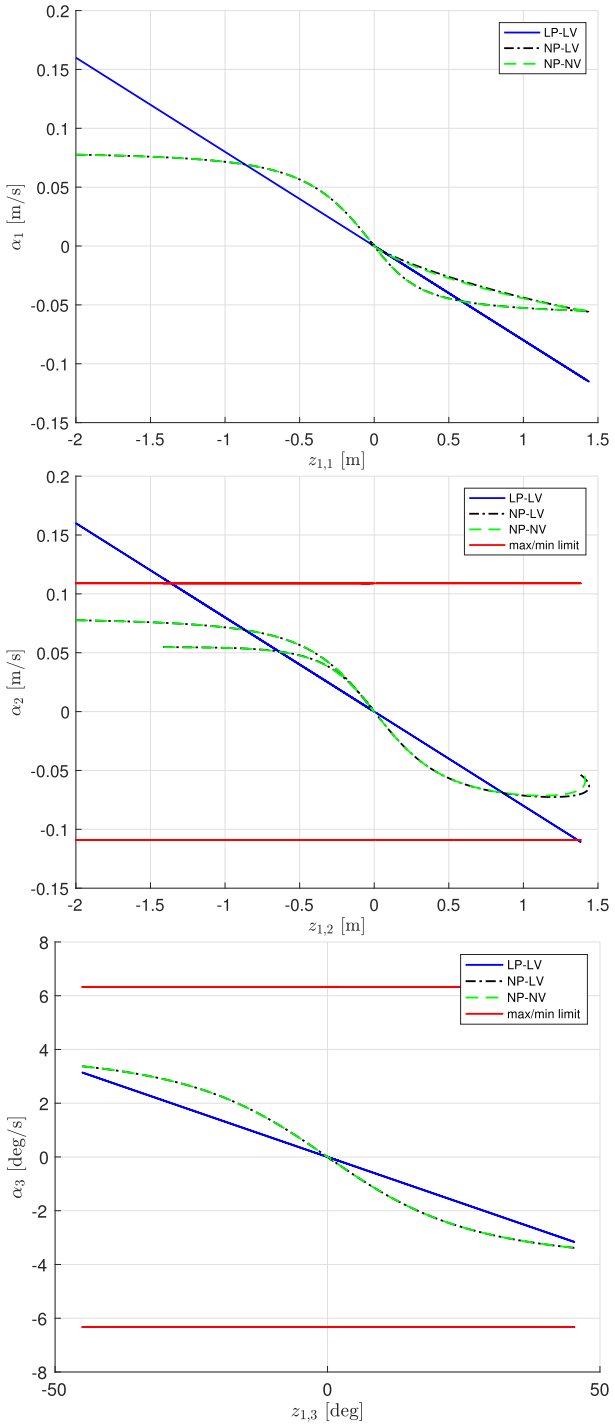

FIGURE 9. The 4-corner simulation: The pose feedback terms as functions of the pose errors.

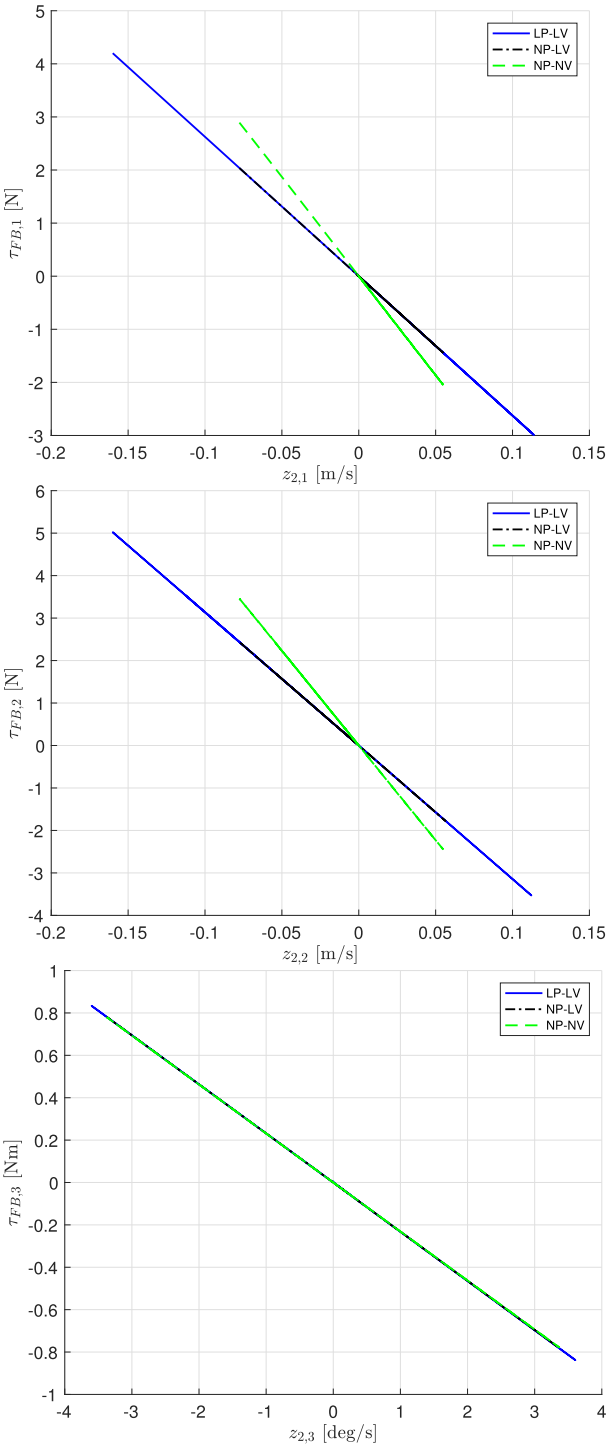

FIGURE 10. The 4-corner simulation: The velocity feedback terms as functions of the velocity errors.

the LP-LV controller's α_2 goes outside the achievable range of the CSAD, while the two nonlinear controllers do not.

Similar to Fig. 9, Fig. 10 shows the feedback contribution for the kinetic part of the three considered controllers. Here, it can been seen that the NP-NV controller has a steeper curve than the two other controllers, which means that it is a bit more aggressive. The plots in figures 9 and 10 correlate with the behavior of the control signals in Fig. 8.

Fig. 11 shows the time evolution of the performance metrics IAE and IAEW of the three controllers. In particular, the IAE plot shows that the LP-LV controller has the poorest performance of three controllers with respect to control accuracy, while the NP-NV controller has the best performance. However, by including the energy use into the performance metric as in IAEW, this result changes such that the NP-LV

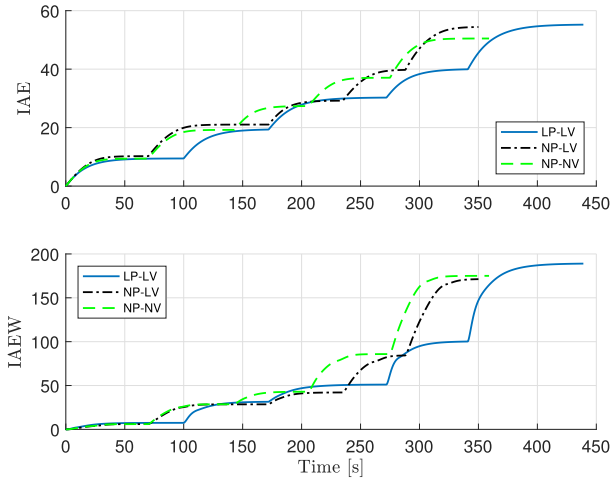

FIGURE 11. The 4-corner simulation: IAE and IAEW performance metrics.

TABLE 2. Final values of the performance metrics for the simulations.

	LP-LV	NP-LV	NP-NV
IAE	55.21	54.35	**50.48**
IAEW	189	**171**	175

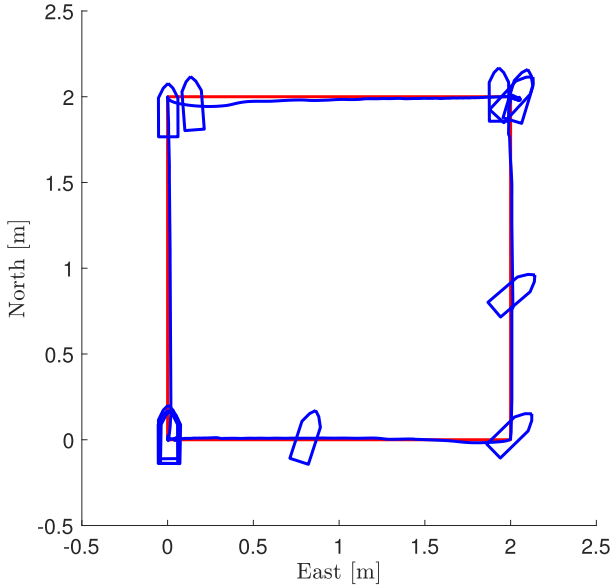

FIGURE 12. The 4-corner experiment: Using LP-LV feedback terms.

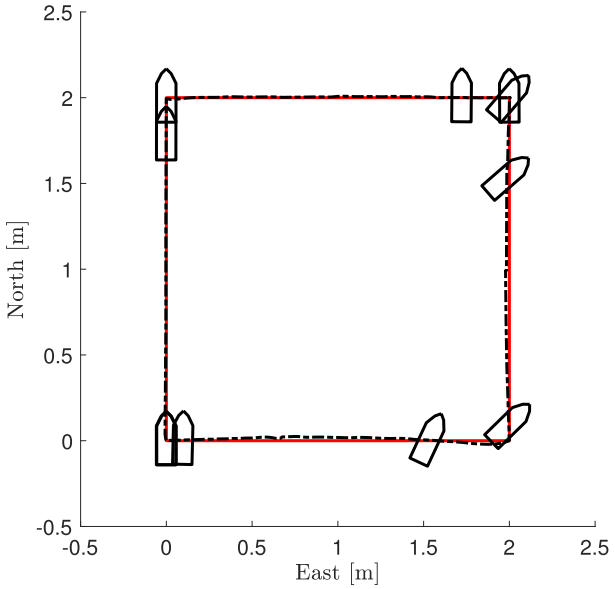

FIGURE 13. The 4-corner experiment: Using NP-LV feedback terms.

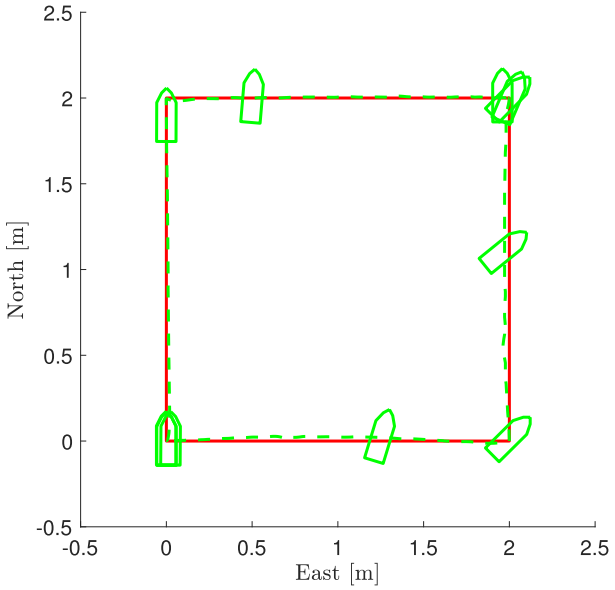

FIGURE 14. The 4-corner experiment: Using NP-NV feedback terms.

controller has the best performance, while the LP-LV controller has the poorest performance. Table 2 shows the final values of the performance metrics for the simulations.

E. EXPERIMENTAL RESULTS

The three controllers have been implemented and experimentally tested on the model-scale ship CSAD [20] in the Marine Cybernetics Laboratory (MC-Lab) at NTNU, for the same 4-corner scenario as in the simulations, see Fig 4. The MC-Lab is equipped with a Qualisys motion capture system in order to measure the pose $\boldsymbol{\eta}$ of the ship. An estimator of the velocity $\boldsymbol{\nu}$ has also been implemented. The control parameters are the same as for the simulations, see Table 1. The controllers are simple to implement and none of them have any significant computational complexity.

Figs. 12-14 show the ship pose and box outlines for the 4-corner test for the LP-LV, NP-LV and NP-NV controllers, respectively. Considering the commanded control inputs of the three controllers, which is shown in Fig. 15, the intensity of the peak values of the control signal is similar to the ones from the simulation shown in Fig. 8. Here, we also see that the three controllers finish the 4-corner test at different times, which is similar to the simulations.

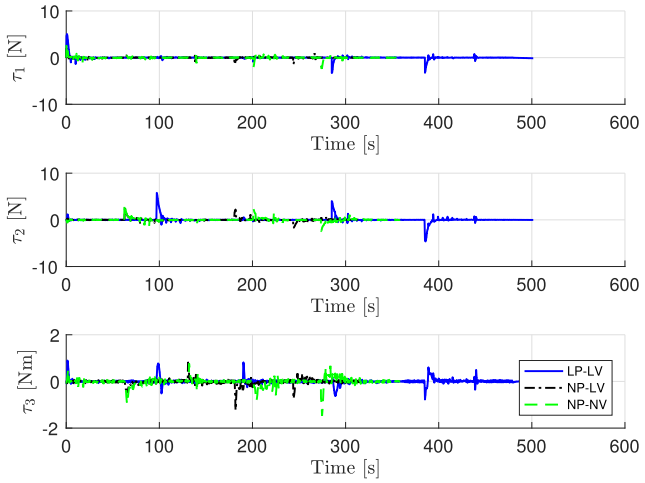

FIGURE 15. The 4-corner experiment: The commanded control inputs.

TABLE 3. Final values of the performance metrics for the experiments.

	LP-LV	NP-LV	NP-NV
IAE	49.92	45.04	**44.92**
IAEW	147.6	**76.14**	102.8

Comparing Fig. 16 with Fig. 9 and Fig. 17 with Fig. 10, similar observations can be made for the experiments as for the simulations.

Fig. 18 shows the performance metrics IAE and IAEW for the three controllers, which also shows a similar result as in the simulations. Table 3 shows the final values of the performance metrics for the experiments.

F. DISCUSSION

This article has shown some additional findings compared to the original findings in [10], using the suggested tuning rules and a different test scenario.

Comparing the results between the simulated and experimental 4-corner tests, similar performance is obtained with respect to the amount of time that the different controllers need to complete the test. Additionally, the NP-NV controller gives the best IAE performance for the considered controllers for both the simulated and experimental tests, while the NP-LV controller consistently uses the least amount of energy among the considered controllers.

Based on the simulation and experimental results, the NP-LV controller comes out on top since it uses the shortest amount of time to complete the 4-corner test. In addition, it has the best energy efficiency as shown by the IAEW metric, and it has a similar tracking performance as the NP-NV controller as shown by the IAE metric. In contrast, the purely linear feedback controller LP-LV uses significantly more time to complete the test, with higher IAE and IAEW as a consequence. Thus, the combined ability to constrain the feedback control input globally while changing the convergence rate locally, for the nonlinear feedback controllers, seems to be advantageous. The price to be paid is the introduction of more tuning parameters, represented by the Δ-parameters, which must be chosen carefully. If they are chosen too small, the control signal will get a discontinuous behavior and can make the control signal exceed the saturation constraints in the linear region.

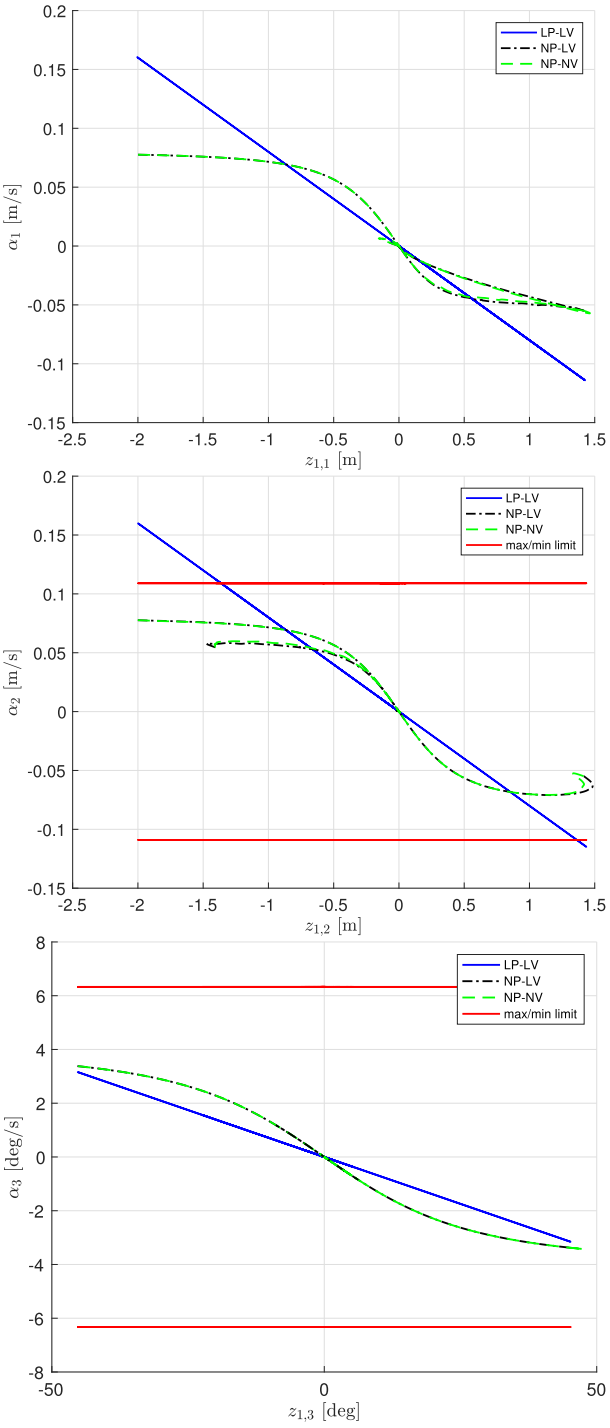

FIGURE 16. The 4-corner experiment: The pose feedback terms as functions of the pose errors.

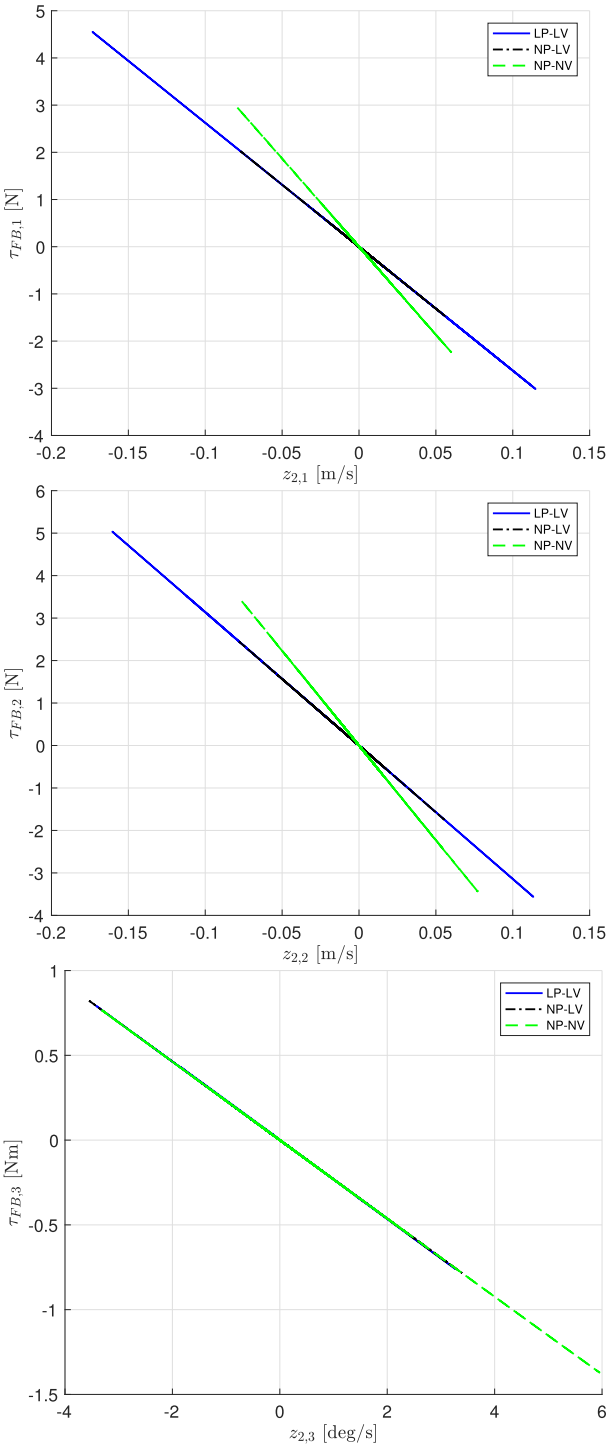

FIGURE 17. The 4-corner experiment: The velocity feedback terms as functions of the velocity errors.

The nonlinear feedback control concept suggested in this article is an initial step toward handling actuator saturation constraints, as well as resulting in improved transient behavior. Also, the cascaded control approach makes it possible to combine the controller with explicit constraint-handling algorithms such as e.g. the dynamic window algorithm [24], as preliminary suggested by the results in [25].

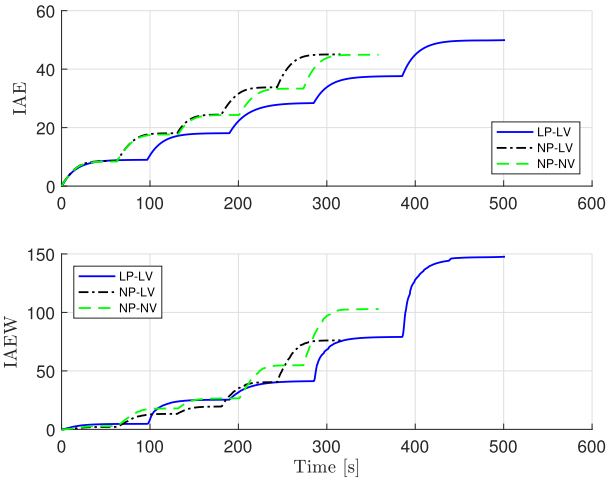

FIGURE 18. The 4-corner experiment: IAE and IAEW performance metrics.

VI. CONCLUSION

This article has further investigated combinations of linear and nonlinear feedback terms for pose and velocity control of ships. Through numerical simulations and model-scale experiments in a ocean basin, three cascaded controllers are compared using performance metrics that consider both control accuracy and energy use. The performance metrics show that the nonlinear feedback controllers outperform the linear baseline controller for the considered step-change maneuvers of the 4-corner test. The combined ability to constrain the feedback control inputs globally and to change the convergence rates locally, for the nonlinear feedback controllers, seems to be advantageous. The price to be paid is the introduction of additional tuning parameters, namely the Δ-parameters. The paper also suggests appropriate tuning rules for the considered controllers. Moreover, stability proofs for the considered closed-loop control systems are provided. Future work includes introducing model uncertainties and unknown disturbances to the ship system. In addition to the mitigation of magnitude saturation constraints considered in this article, it is also relevant to consider how actuator rate saturation constrains can be handled.

ACKNOWLEDGMENT

The authors gratefully acknowledge Senior Engineer Torgeir Wahl and Ph.D. candidate Andreas R. Dahl at NTNU's Department of Marine Technology for valuable support during the experiments.

REFERENCES

[1] N. Minorsky, "Directional stability of automatically steered bodies," *J. Amer. Soc. Nav. Eng.*, vol. 34, no. 2, pp. 280–309, Mar. 2009.

[2] T. I. Fossen and J. P. Strand, "Tutorial on nonlinear backstepping: Applications to ship control," *Model., Identificat. Control, Norwegian Res. Bull.*, vol. 20, no. 2, pp. 83–135, 1999.

[3] T. I. Fossen, "Nonlinear passive control and observer design for ships," *Model., Identificat. Control, Norwegian Res. Bull.*, vol. 21, no. 3, pp. 129–184, 2000.

[4] J. E. Refsnes, A. J. Sorensen, and K. Y. Pettersen, "Model-based output feedback control of slender-body underactuated AUVs: Theory and experiments," *IEEE Trans. Control Syst. Technol.*, vol. 16, no. 5, pp. 930–946, Sep. 2008.

[5] T. I. Fossen, *Handbook of Marine Craft Hydrodynamics and Motion Control*. Hoboken, NJ, USA: Wiley, 2011.
[6] T. I. Fossen, M. Breivik, and R. Skjetne, "Line-of-sight path following of underactuated marine craft," in *Proc. 6th IFAC Conf. Manoeuvring Control Mar. Craft*, Girona, Spain, 2003.
[7] M. Breivik, J. P. Strand, and T. I. Fossen, "Guided dynamic positioning for fully actuated marine surface vessels," in *Proc. 7th IFAC Conf. Manoeuvring Control*, Lisbon, Portugal, 2006, pp. 1–6.
[8] M. Breivik and T. I. Fossen, "Applying missile guidance concepts to motion control of marine craft," in *Proc. 7th IFAC Conf. Control Appl. Marine Syst.*, Bol, Croatia, 2007.
[9] M. Breivik and T. I. Fossen, "Guidance laws for autonomous underwater vehicles," in *Underwater Vehicles*, A. V. Inzartsev, Ed. In-Tech Education and Publishing, 2009, pp. 51–76.
[10] M. E. N. Sørensen and M. Breivik, "Comparing combinations of linear and nonlinear feedback terms for motion control of marine surface vessels," in *Proc. 10th IFAC Conf. Control Appl. Mar. Syst.*, Trondheim, Norway, 2016, pp. 1–8.
[11] O. N. Lyngstadaas, T. E. Saeterdal, M. E. N. Sorensen, and M. Breivik, "Improvement of ship motion control using a magnitude-rate saturation model," in *Proc. IEEE Conf. Control Technol. Appl. (CCTA)*, Copenhagen, Denmark, Aug. 2018, pp. 75–81.
[12] X.-K. Zhang and G.-Q. Zhang, "Design of ship course-keeping autopilot using a sine function-based nonlinear feedback technique," *J. Navigat.*, vol. 69, no. 2, pp. 246–256, Mar. 2016.
[13] Q. Zhang and X. Zhang, "Nonlinear improved concise backstepping control of course keeping for ships," *IEEE Access*, vol. 7, pp. 19258–19265, 2019.
[14] Y. Deng, X. Zhang, N. Im, G. Zhang, and Q. Zhang, "Adaptive fuzzy tracking control for underactuated surface vessels with unmodeled dynamics and input saturation," *ISA Trans.*, vol. 103, pp. 52–62, Aug. 2020.
[15] M. E. N. Sørensen and M. Breivik, "Comparing nonlinear adaptive motion controllers for marine surface vessels," in *Proc. 10th IFAC Conf. Manoeuvring Control Mar. Craft*, Copenhagen, Denmark, 2015.
[16] M. Arcak, M. Seron, J. Braslavsky, and P. Kokotovic, "Robustification of backstepping against input unmodeled dynamics," *IEEE Trans. Autom. Control*, vol. 45, no. 7, pp. 1358–1363, Jul. 2000.
[17] F. Lamnabhi-Lagarrigue, E. Panteley, E. Lefeber, and A. Loría, *Advanced Topics in Control Systems Theory: Lecture Notes from FAP 2004*. Springer, 2005.
[18] H. K. Khalil, *Nonlinear Systems*. Upper Saddle River, NJ, USA: Prentice-Hall, 2002.
[19] A. Pavlov, H. Nordahl, and M. Breivik, "MPC-based optimal path following for underactuated vessels," in *Proc. 8th IFAC Conf. Manoeuvring Control Mar. Craft*, Guarujá, Brazil, 2009.
[20] J. Bjørnø, H.-M. Heyn, R. Skjetne, A. R. Dahl, and P. Frederich, "Modeling, parameter identification and thruster-assisted position mooring of C/S Inocean CAT I Drillship," in *Proc. 36th Int. Conf. Ocean, Offshore Arctic Eng.*, Trondheim, Norway, Jun. 2017, pp. 1–10.
[21] B.-O. H. Eriksen and M. Breivik, "Modeling, identification and control of high-speed ASVs: Theory and experiments," in *Sensing and Control for Autonomous Vehicles: Applications to Land, Water and Air Vehicles*. Springer, 2017, pp. 407–431.
[22] R. Skjetne, M. E. N. Sørensen, M. Breivik, S. A. T. Værnø, A. H. Brodtkorb, A. J. Sørensen, O. K. Kjerstad, V. Calabrò, and B. O. Vinje, "AMOS DP research cruise 2016: Academic full-scale testing of experimental dynamic positioning control algorithms onboard R/V Gunnerus," in *Proc. 36th Int. Conf. Ocean, Offshore Arctic Eng.*, vol. 1. Trondheim, Norway: Offshore Technology, 2017, pp. 1–10.
[23] O. N. Lyngstadaas, "Ship motion control concepts considering actuator constraints," MSc thesis, Dept. Eng. Cybern., Norwegian Univ. Sci. Technol., Trondheim, Norway, 2018.
[24] D. Fox, W. Burgard, and S. Thrun, "The dynamic window approach to collision avoidance," *IEEE Robot. Autom. Mag.*, vol. 4, no. 1, pp. 23–33, Mar. 1997.
[25] M. E. N. Sorensen, M. Breivik, and B.-O.-H. Eriksen, "A ship heading and speed control concept inherently satisfying actuator constraints," in *Proc. IEEE Conf. Control Technol. Appl. (CCTA)*, Mauna Lani, HI, USA, Aug. 2017, pp. 323–330.

MIKKEL ESKE NØRGAARD SØRENSEN received the M.Sc. degree in electrical engineering from the Technical University of Denmark (DTU), Lyngby, Denmark, in 2014. He is currently pursuing the Ph.D. degree in engineering cybernetics with the Norwegian University of Science and Technology (NTNU), Trondheim, Norway. He is also working at MAN Energy Solutions. His research interest includes nonlinear and adaptive motion control of unmanned vehicles.

MORTEN BREIVIK (Member, IEEE) received the M.Sc. and Ph.D. degrees in engineering cybernetics from NTNU, in 2003 and 2010, respectively. He is currently the Head of the NTNU's Department of Engineering Cybernetics and an Associate Researcher with the Centre for Autonomous Marine Operations and Systems (NTNU AMOS). He has previously worked as an Assistant Professor and a Researcher at NTNU, a Scientific Advisor at Maritime Robotics, and a Principal Engineer and the Department Manager of Applied Cybernetics at Kongsberg Maritime. His research interest includes nonlinear and adaptive motion control of unmanned vehicles in general and autonomous ships in particular. He is also a member of the Norwegian Board of Technology.

ROGER SKJETNE (Member, IEEE) received the M.Sc. degree from the University of California at Santa Barbara (UCSB), in 2000, and the Ph.D. degree in control engineering from the Norwegian University of Science and Technology (NTNU), in 2005. He holds the Exxon Mobil Prize for his Ph.D. thesis at NTNU. Prior to his studies, he worked as a Certified Electrician at Aker Elektro AS, worked on numerous oil installations for the North Sea, and from 2004 to 2009, he was employed at Marine Cybernetics AS, working on hardware-in-the-loop simulation for verification of marine control systems. Since August 2009, he has been holding the Kongsberg Maritime Chair of Professor in Marine Control Engineering at the Department of Marine Technology, NTNU. From 2017 to 2018, he was a Visiting Research Scholar with the Center for Control, Dynamical Systems and Computation, UCSB. His research interests include dynamic positioning of marine vessels, Arctic stationkeeping and ice management systems, control of shipboard hybrid electric power systems, nonlinear motion control of marine vehicles, and autonomous ships and marine robots.